

# V515 And: An Intermediate Polar in the Period Gap Exhibiting Outbursts

Srinivas M Rao,<sup>1,2\*</sup> Jeewan C Pandey<sup>1†</sup>, Nikita Rawat<sup>3</sup>, Simone Scaringi<sup>4</sup>, Arti Joshi<sup>5</sup>, David A. H. Buckley<sup>3</sup>, and Ajay Kumar Singh<sup>6</sup>

<sup>1</sup>*Aryabhata Research Institute of Observational Sciences (ARIES), Nainital 263001, India*

<sup>2</sup>*Mahatma Jyotiba Phule Rohilkhand University, Bareilly 243006, India*

<sup>3</sup>*South African Astronomical Observatory, PO Box 9, Observatory, Cape Town, 7935, South Africa*

<sup>4</sup>*Centre for Extragalactic Astronomy, Department of Physics, Durham University, South Road, Durham DH1 3LE, UK*

<sup>5</sup>*Institute of Astrophysics, Pontificia Universidad Católica de Chile, Av. Vicuña Mackenna 4860, 7820436 Macul, Santiago, Chile*

<sup>6</sup>*Department of Applied Physics/Physics, Bareilly College, Bareilly-243001, India*

Accepted XXX. Received YYY; in original form ZZZ

## ABSTRACT

Using long-term observations from the Transiting Exoplanet Survey Satellite (TESS) along with spectroscopic observations from the 3.6 m Devasthal Optical Telescope (DOT), we present a comprehensive time-series and spectral analysis of the intermediate polar V515 And. Our analysis reveals that V515 And resides within the period gap, with the detection of its orbital period of 2.73116 h. Additionally, we confirm the earlier findings of the spin and beat periods to be 465.4721 s and 488.6067 s, respectively. The time-resolved timing analysis reveals that V515 And undergoes changes in its accretion geometry, not only between different TESS sectors but also within individual sector observations. The system exhibits a transition in the dominant accretion mode, switching between disc-fed and stream-fed accretion. In the TESS light curve, we identify two successive outburst-like episodes, each persisting for roughly a day and reaching peak luminosities of  $2.7 \times 10^{33}$  and  $1.9 \times 10^{33}$  erg s<sup>-1</sup>. Our analysis suggests that these bursts belong to the recently proposed class of micronovae. The optical spectrum of V515 And is characterised by strong Balmer and He II emission lines and shows an inverse Balmer decrement indicating the magnetic nature of the source.

**Key words:** accretion, accretion discs; cataclysmic variables-stars: individual: V515 And; stars: individual: V515 And;

## 1 INTRODUCTION

Intermediate polars (IPs) are a subclass of the magnetic cataclysmic variable (MCVs) where the magnetic field strength of the primary component of the binary, white dwarf (WD), ranges from ~0.1 to 10 megagauss (MG) and accretes mass from the secondary red dwarf (Patterson 1994). Due to the influence of the magnetic field of the WD, the accreted material accumulates near the magnetic poles. The accretion regime is either via disc, stream, or both. The disc-fed accretion occurs via a Keplerian disc, and this disc is disrupted at a specific point known as the magnetospheric radius of WD, and from this point, the material follows the magnetic field lines of the WD (Hellier et al. 1989a). In contrast, in the stream-fed accretion, the material is directly accreted onto the magnetic poles of the WD following the magnetic field lines (Rosen et al. 1988). In stream-fed accretion, if the material skims over the disc and accretes through the disc as well, then the accretion is called disc overflow (Hellier et al. 1989b). The power at the spin ( $\omega$ ) and the beat ( $\omega - \Omega$ ) frequencies in the power spectra help us identify the probable accretion geometry of the system (Hellier 1991, 1993b). The magnetically channelled accretion column free-falls with supersonic velocities close to the surface of the WD, which leads to the formation of shocks. X-rays are emitted in the post-shock region as the matter cools via thermal

bremsstrahlung and cyclotron radiation (Aizu 1973; Wu et al. 1994; Cropper et al. 1999). The X-rays may be reprocessed from other regions of the WD, such as the WD itself or the accretion disc surrounding it, resulting in optical emission.

The orbital period ( $P_\Omega$ ) of IPs generally ranges from 1.35–48 h<sup>1</sup>. There is a significant dearth of sources in the 2–3 h range, and this is known as the period gap (Warner & Wickramasinghe 1991). However, the IP Paloma with a spin-to-orbital period ratio of 0.83 was the only earlier known source in the period gap (Schwarz et al. 2007; Joshi et al. 2016). This period gap is also observed for non-magnetic cataclysmic variables (NMCVs), but it is less obvious in the case of polars (Schreiber et al. 2024). Recent studies by Schreiber et al. (2024) have refined the boundaries of the period gap in CVs to 2.45–3.18 hrs. The onset of the period gap is explained by the disruptive magnetic braking (DMB) model, which indicates a significant decrease or complete cessation of mass transfer from the secondary. Gravitational radiation brings the stars closer together, allowing mass transfer to resume at a much lower rate (Kolb 1993).

In this paper, we investigate the accretion properties of V515 And (= XSS J00564+4548), a system that appears to reside within the period gap. It was identified in the RXTE all-sky survey with the spin period ( $P_\omega$ ) of the WD as ~480 s (Bikmaev et al. 2006). Butters et al. (2008) found  $P_\omega$  to be  $465.68 \pm 0.07$  s and also obtained a

\* E-mail: srinivas@aries.res.in, srinivas22546@gmail.com

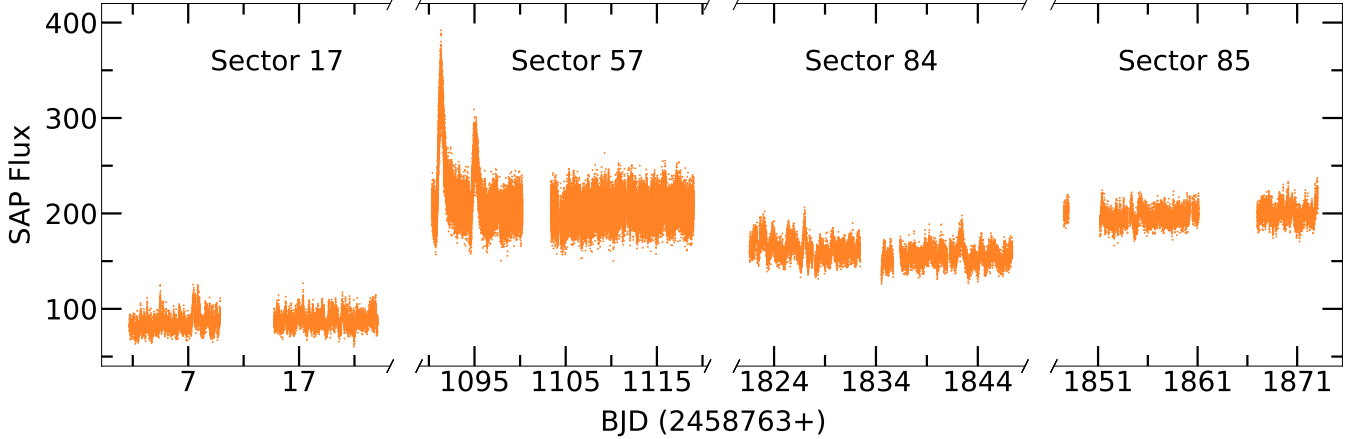
† E-mail: jeewan@aries.res.in

<sup>1</sup> <https://asd.gsfc.nasa.gov/Koji.Mukai/iphone/catalog/alpha.html>

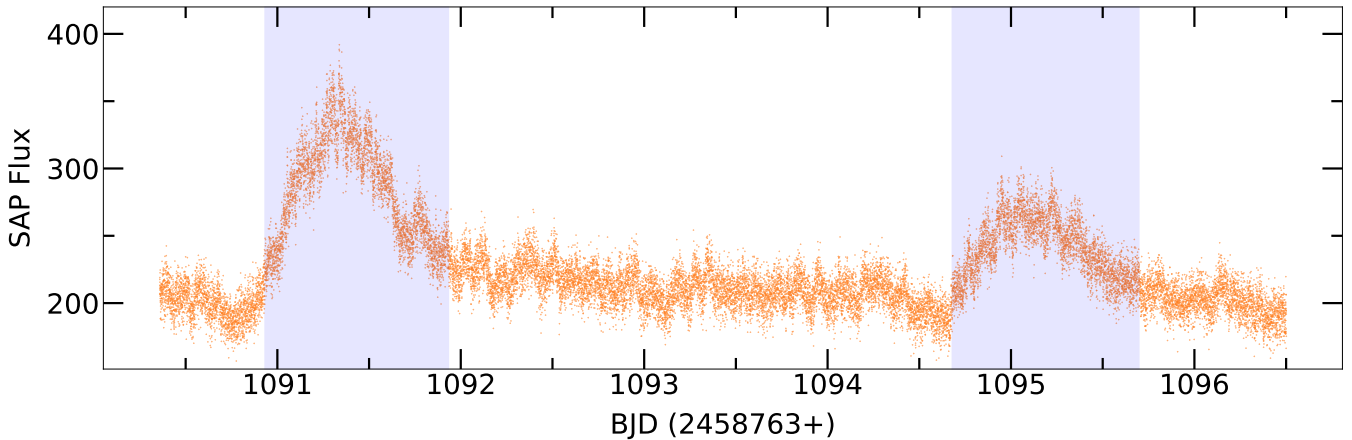
**Table 1.** Log of observations of V515 And using TESS.

Sector	Start Date of Obs. (YYYY-MM-DD)	Start Time of Obs. (UT)	End Date of Observation (YYYY-MM-DD)	End Time of Observation (UT)
17	2019-10-08	04:29:46	2019-11-02	04:22:01
57*	2022-09-30	20:34:42	2022-10-29	14:51:17
84	2024-10-01	02:13:36	2024-10-26	20:16:09
85	2024-10-27	01:24:09	2024-11-21	13:09:25

\* The data is available for both 120 and 20 s cadence.



(a) TESS light curve



(b) Outburst

**Figure 1.** (a) TESS light curve of all sectors. (b) Zoomed-in section from sector 57 showing the two outbursts in shaded regions.

probable beat period ( $P_{\omega-\Omega}$ ) of  $489.0 \pm 0.7$  s. However, [Bonnet-Bidaud et al. \(2009\)](#) found a different  $P_{\omega}$  in X-rays of  $469.75 \pm 0.26$  s. Based on approximately 1.3 years of white light observations separated by a one-year gap, [Kozhevnikov \(2012\)](#) reported refined values for the  $P_{\omega}$  and  $P_{\omega-\Omega}$  of V515 And as  $465.48493 \pm 0.00007$  s and  $488.61822 \pm 0.00009$  s, respectively. Using these results, the orbital period ( $P_{\Omega}$ ) of V515 And is estimated to be between 2.62 and 2.73 h, which places it in the period gap. This finding necessitates further investigation of V515 And using high-cadence, long-baseline TESS data. The presence of two outburst-like features in the TESS light curve further motivated us to do this study.

We organise the paper as follows: in section 2, we describe the observations and data. Section 3 contains the analysis and results.

Finally, we present the discussion and conclusions in sections 4 and 5, respectively.

## 2 OBSERVATIONS AND DATA

### 2.1 Timing observations

V515 And was observed by TESS for four sectors. The log of observations is given in Table 1. The TESS ([Ricker et al. 2015](#)) instrument consists of four wide-field CCD cameras that can image a region of the sky, measuring  $24^{\circ} \times 96^{\circ}$ . TESS observations are broken up into sectors, each lasting two orbits, or about 27.4 days and conduct their downlink of data while at perigee. This results in a small gap in the

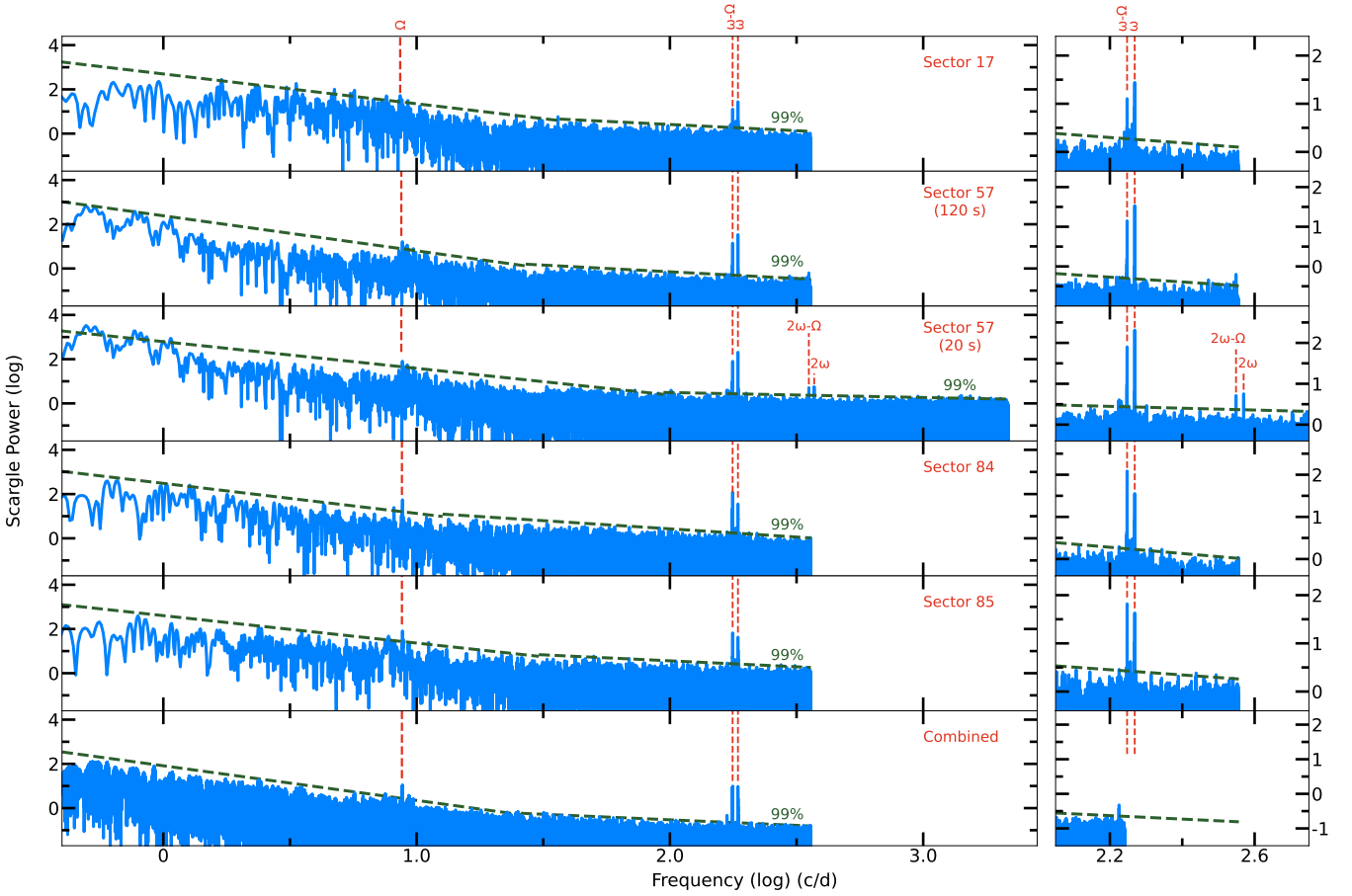


**Figure 2.** TESS power spectra of different sectors and the combined dataset. The identified frequencies are marked with red vertical dashed lines. The green dashed line represents the 99% confidence level. The right panel shows the zoomed-in part near the  $\omega$  and  $\omega - \Omega$  frequencies.

data compared to the overall run length. The data is stored in the Mikulski Archive for Space Telescopes data<sup>2</sup> with unique identification number ‘TIC 196278926’. TESS provides data in two forms, namely Simple Aperture Photometry (SAP) flux and the pipeline-processed Pre-search Data Conditioned Simple Aperture Photometry (PDCSAP) flux. PDCSAP flux is the SAP flux values corrected for instrumental variations<sup>3</sup>. While performing corrections in the SAP flux values, the pipeline can sometimes also remove systematic trends (Jenkins et al. 2016). Hence, for our analysis, we have used SAP flux, which had quality flags marked as ‘0’.

## 2.2 Spectroscopic observations

Spectroscopic observations of V15 And were taken using the ARIES-Devasthal Faint Object Spectrograph and Camera (ADFOSC; Omar et al. 2019), mounted on the 3.6 m Devasthal optical telescope (DOT; Kumar et al. 2018). It is comprised of a 4k × 4k deep-depletion CCD camera providing a 0.2 arcseconds/pixel scale with a 2 × 2 binning (Panchal et al. 2023). The observations were done with a slit 1.5" wide and 8" long and a 132R-600 gr/mm grism which covers a wavelength

range of 3500-7000 Å, centred at 4880 Å. A total of three spectra were obtained on three consecutive nights - 25, 26 and 27th January 2025, each having an exposure of 40 min. These data were obtained ~4 months after the last TESS Sector 85 observation. The bias and flat frames were taken for pre-processing, and the HgAr lamp was used for wavelength calibration. For flux calibration, a standard star (HZ 2) was observed on the same night, using the same slit and grism configurations as those for the source. The reduction was done using Image Reduction and Analysis Facility (IRAF) software (Tody 1986, 1993).

## 3 ANALYSIS AND RESULTS

### 3.1 Timing analysis

#### 3.1.1 Light curve and power spectra

The combined light curve of V515 And from all sectors’ observation is shown in 1(a). The variability in the light curve is clearly visible. Two burst-like features in the light curve of sector 57, lasting ~1 day, were noticed and shown in 1(b). To determine the periodicities of the underlying variabilities, the Lomb-Scargle (LS) periodogram method (Lomb 1976; Scargle 1982) was applied to the light curves of the individual sectors and the combined dataset from all sectors. For sector 57, the burst duration in the light curve was removed for the periodogram analysis. The significance of peaks within the power

<sup>2</sup> <https://mast.stsci.edu/portal/Mashup/Clients/Mast/Portal.html>

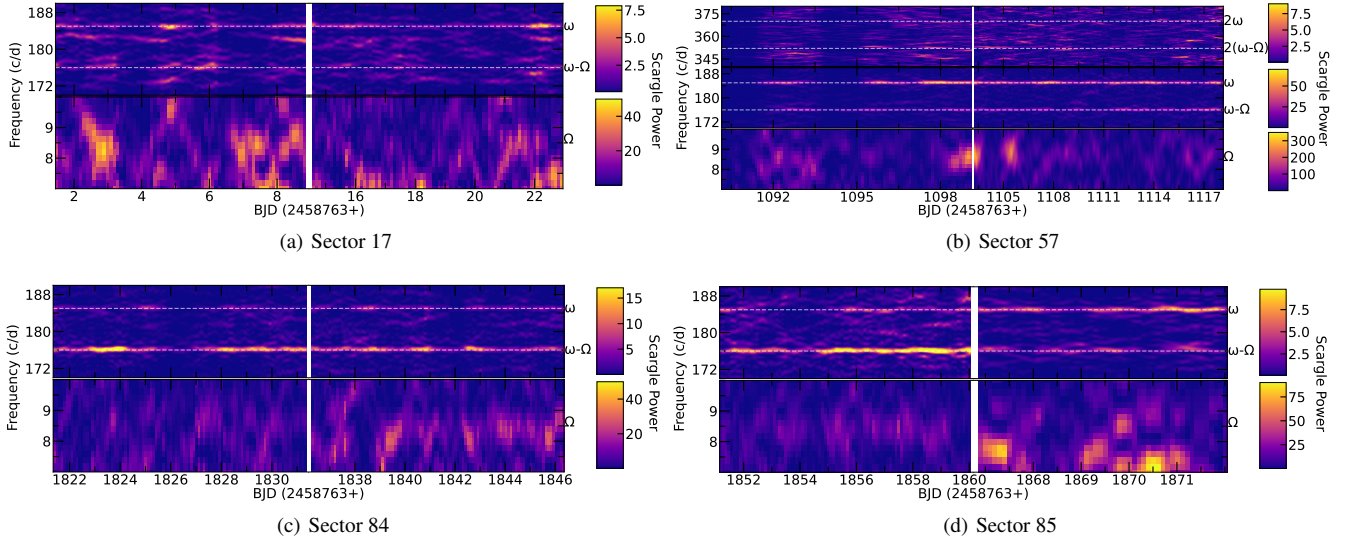
<sup>3</sup> See section 2.1 of the TESS archive manual at <https://outerspace.stsci.edu/display/TESS/2.1+Levels+of+data+processing>

**Table 2.** Periods obtained corresponding to the dominant peaks of the LS power spectra of TESS.

Sector	Cadence (s)	$P_{\Omega}$ (h)	$P_{\omega}$ (s)	$P_{\omega-\Omega}$ (s)	$P_{2\omega}$ (s)	$P_{2(\omega-\Omega)}$ (s)
17	120	$2.740 \pm 0.003$	$465.46 \pm 0.03$	$488.60 \pm 0.03$	-	-
57	120	$2.731 \pm 0.002$	$465.46 \pm 0.02$	$488.59 \pm 0.02$	-	-
57	20	$2.731 \pm 0.003$	$465.46 \pm 0.02$	$488.59 \pm 0.02$	$232.735 \pm 0.005$	$244.296 \pm 0.006$
84	120	$2.728 \pm 0.003$	$465.47 \pm 0.02$	$488.62 \pm 0.03$	-	-
85	120	$2.731 \pm 0.003$	$465.46 \pm 0.02$	$488.56 \pm 0.02$	-	-
Mean*		$2.731 \pm 0.001$	$465.46 \pm 0.01$	$488.59 \pm 0.01$	-	-
Combined <sup>†</sup>		$2.73116 \pm 0.00004^*$	$465.4721 \pm 0.0003$	$488.6067 \pm 0.0004$	-	-

\* Weighted mean and corresponding weighted error of periods derived from different sectors.

<sup>†</sup> Represents the periods derived from the power spectra of combined TESS observations of all sectors.

**Figure 3.** Trailing power spectra from TESS, binned using a 1-day moving window with a step size of 0.1 days. The  $\omega$ , and  $\omega - \Omega$  frequencies, along with their identified harmonics, are shown with dashed lines.

spectra was determined using the methodology described by [Vaughan \(2005\)](#), assuming that TESS power spectra possess different types of noise ([Kálmán et al. 2025](#)). We have only considered those peaks which were above the 99% significance level. The power spectra for all the sectors are shown in Figure 2.

We primarily identified three significant frequencies at 8.87, 176.84, and 185.62 cycles/day (c/d) in all sectors as well as the combined dataset, which are designated as orbital ( $\Omega$ ),  $\omega - \Omega$ , and  $\omega$ , respectively. Recently, [Bruch \(2025\)](#) also obtained these frequencies in his analysis. In the combined dataset, the  $\omega$  and  $\omega - \Omega$  frequencies have almost equal power. However, in sectors 17 and 57, the  $\omega$  and in sectors 84 and 85, the  $\omega - \Omega$  were found to be dominant frequencies in the power spectra. We identified that the  $\Omega$  frequency of the system is consistent with the inferred  $\Omega$  frequency using the  $\omega$  and  $\omega - \Omega$  frequencies. In addition to the above-mentioned frequencies, the power spectral analysis of the 20 s cadence data of sector 57 also shows the presence of harmonics of  $\omega$  and  $\omega - \Omega$  frequencies. A few other frequencies towards the bluer end of the power spectra were found above the significance level, but none of these frequencies were consistent among the power spectra of all sectors. Furthermore, none of these frequencies were present in the combined power spectra. Therefore, we have not considered them for any further analysis. The periods corresponding to these frequencies are given in Table 2. We have also calculated the weighted mean and corresponding weighted

error for all periods across different sectors, which are consistent with those derived from the combined data set.

### 3.1.2 Trailed power spectra

As the dominance of  $\omega$  and  $\omega - \Omega$  frequencies varied across power spectra of different sectors' data, a trailing power spectrum was calculated to study their evolution. Figure 3 shows the trailed power spectra of all four sectors of TESS observations. To obtain the trailed power spectra, we chose a window size of 1 day and moved it in increments of 0.1 day. We have shown only the frequency regions around which we obtained the  $\Omega$ ,  $\omega$ , and  $\omega - \Omega$  frequencies in the sector-wise power spectra. For sector 57, we show results for a 20 s cadence (see Figure 3(b)), which also includes frequencies at  $2\omega$  and  $2(\omega - \Omega)$ . In each sector, the  $\Omega$  frequency was detected only in a few days. In sectors 17 and 57, the  $\omega$  frequency was more dominant than the  $\omega - \Omega$  frequency on most days; however, in sector 84, the  $\omega - \Omega$  frequency was more dominant on most days. The results for the 120 s cadence dataset in sector 57 were similar to those for the 20 s cadence dataset. Following sector 84, in the first half of sector 85,  $\omega - \Omega$  frequency remained dominant, whereas in the 2nd half, the dominance again switched to  $\omega$  frequency. During the period of bursts, there was the absence of both  $\omega$  and  $\omega - \Omega$  frequencies. The power of  $\omega$  and  $\omega - \Omega$  frequencies gradually decreases before the

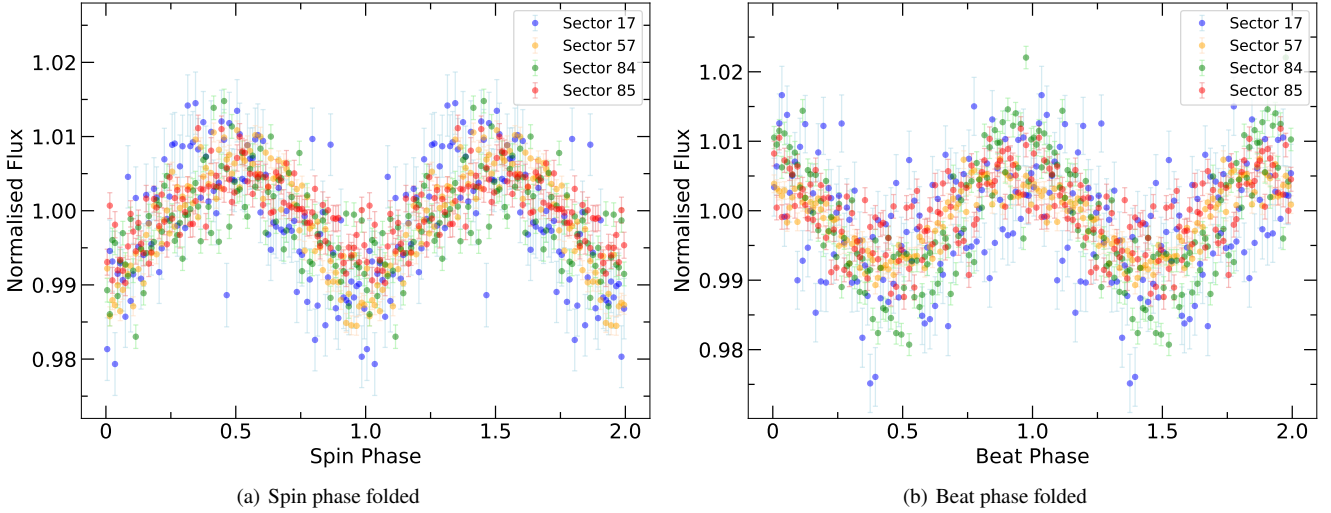


**Figure 4.** Spin and beat phase folded light curves of V515 And for each observed sector.

onset of the second burst, and then the power of both frequencies gradually increases after the end of the outburst.

### 3.1.3 Phase-folded light curves and pulse fraction

Light curves were folded over  $P_\omega$  and  $P_{\omega-\Omega}$ , which were obtained from the combined dataset using the ephemeris given by (Kozhevnikov 2012). The spin- and beat-phase-folded light curves for all sectors are shown in Figures 4(a) and 4(b), respectively. To make the trailed phase-folded light curve, we have followed a similar methodology to that discussed in Section 3.1.2 for obtaining trailed power spectra. The trailed spin and beat phase folded light curves of all the sectors are shown in Figure 5(a) and 5(b), respectively. A single peak pattern was observed in both phase-folded light curves, which was centred around 0.5 phase in spin-phased light curves and  $\sim 0.9$  phase in beat-phased light curve. For each phased light curve, we have derived the pulse fraction (PF) as

$$PF = \frac{A_{max} - A_{min}}{A_{max} + A_{min}} \times 100\% \quad (1)$$

Here,  $A_{max}$  and  $A_{min}$  are the maximum and minimum flux of the day-wise phased light curve, which were obtained by fitting a sinusoid on that phased light curve. The spin and beat pulse fraction for all the sectors is shown in Figure 5(c). In sector 17, the spin and beat pulse fractions were comparable, but on a few days, the spin pulse fraction was higher. In contrast, in the latter sectors, a distinction is observed between the values of spin and beat pulse fractions. On the majority of days in sector 57, the spin pulse fraction was dominant, whereas in sector 84, the beat pulse fraction was dominant. During the first half of sector 85, the beat pulse fraction was dominant, and in the latter half, the dominance changed to the spin pulse fraction.

### 3.1.4 Characterising the Outbursts

Though the TESS excels in providing precise relative photometry, it is advantageous to utilise data from another observatory to obtain absolute photometry from TESS observations. To convert the TESS data into flux, we need to calibrate them using simultaneous ground-based observations, following a methodology similar to that applied

by several authors in the past (such as Scaringi et al. 2022b; Hkiewicz et al. 2024; Irving et al. 2024; Veresvarska et al. 2024, 2025). We have used the simultaneous ASAS-SN g-band data for calibration. The g-band is centred at 477 nm and has a width of 100 nm. As the outbursts were present in sector 57, the availability of 20 s cadence data for that sector allowed us to calibrate with ground-based photometry. We have selected only those ASAS-SN g-band data points that were obtained within 20 s of the TESS observations. The calibration was done for each half of the sector separately. Then, we fit a linear relationship between the two bands, and a direct conversion can be established by the relation

$$F_{ASAS-SN\ g}(Jy) = A \times F_{TESS}(e^- s^{-1}) + C \quad (2)$$

This converts the TESS count rates into the ASAS-SN g-band magnitude. From the *Gaia* DR3 parallax (Gaia Collaboration et al. 2023), the distance of the source is calculated as  $958 \pm 24$  pc. Using the distance and TESS's bandwidth (500 nm), we calculated the luminosity in the g-band. The luminosity obtained here is underestimated because we have not considered any bolometric correction when cross-calibrating ASAS-SN and TESS, and we have assumed a flat emission spectrum while converting from spectral flux density to luminosity.

We have used the Bayesian Block algorithm (Scargle 1998; Scargle et al. 2013) to identify the start and end times of the outburst. The start and end times of the first outburst were found to be BJD 2459453.9321 and 2459854.933, respectively; whereas to those of the 2nd outburst were BJD 2459857.678 and 2459858.697, respectively. The durations of the first and second outbursts were found to be 1.001 and 1.019 days, respectively. Both outbursts have a fast rise and slow decline, and there is a dip before the start of both outbursts. The first outburst was found to have a higher amplitude than the latter. The peak optical luminosity of the first outburst was found to be  $(2.7 \pm 0.5) \times 10^{33}$  erg  $s^{-1}$  and that of the second outburst was found to be  $(1.9 \pm 0.4) \times 10^{33}$  erg  $s^{-1}$ . We have estimated the baseline luminosity during the burst by using luminosity values from the non-outburst phase. A running mean was computed, and the gaps were interpolated using the spline function. We then subtract this baseline luminosity from the calibrated light curve. By integrating this baseline-subtracted luminosity during the outburst, we have obtained the total energy of the bursts. The energy of the first outburst

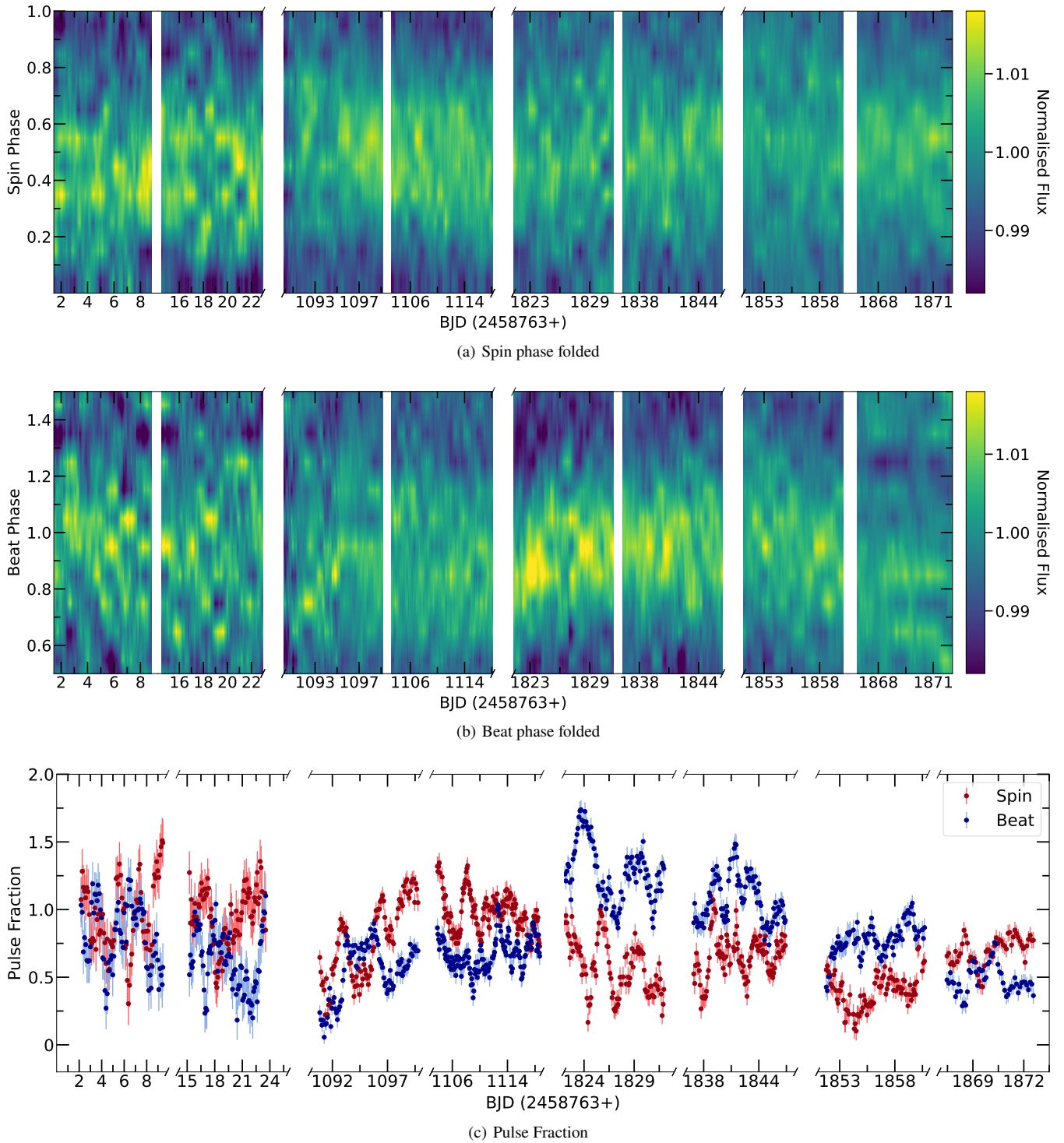


**Figure 5.** (a) and (b) Trained spin and beat phase folded light curve of the entire dataset. (c) Variation of spin and beat pulse fraction.

was determined to be  $(6.0 \pm 0.1) \times 10^{37}$  erg, whereas that of the 2nd outburst was determined to be  $(2.9 \pm 0.1) \times 10^{37}$  erg.

### 3.2 Optical spectra

Optical spectra at three epochs of observation are shown in Figure 6. At all three epochs, the spectrum is dominated by Balmer emission

lines from  $H_\alpha$  to  $H_\delta$ . We have identified several lines of He I and Bowen fluorescence, as well as a couple of He II lines. The blend of the Na D1 and D2 lines exhibits an absorption feature. A single Gaussian was fitted to obtain the properties of the emission lines. The fluxes, FWHM, and equivalent width (EW) of the emission lines are given in Table 3. The flux of He II 4686 varies during the course of three nights, and the FWHM steadily increases. The

**Table 3.** Identification, flux, EW, and FWHM for emission features of the observed spectra of V515 And at three different epochs.

Identification	25th January			26th January			27th January		
	Flux	-EW	FWHM	Flux	-EW	FWHM	Flux	-EW	FWHM
H $\gamma$ (4340 Å)	5.2	5.88	922	3.9	4.13	815	3.3	4.66	818
C III/N III (4640/50 Å)	1.8	3.0	1217	2.0	3.17	1210	1.2	2.29	1094
He II (4686 Å)	2.3	4.01	842	2.6	3.99	923	2.2	4.19	1141
H $\beta$ (4861 Å)	4.2	7.91	835	3.7	6.80	797	3.9	7.41	820
He I (4922 Å)	0.5	1.03	657	0.4	0.69	487	0.4	0.82	503
He I (5875 Å)	0.9	3.33	726	1.0	3.50	682	1.0	3.65	714
H $\alpha$ (6563 Å)	3.9	17.56	793	3.5	14.64	747	3.8	17.55	776
He I (6678 Å)	0.5	2.71	697	0.6	2.9	874	0.6	2.94	722

Note. Flux, EW, and FWHM are in the unit of  $10^{-14}$  erg cm $^{-2}$  s $^{-1}$ , Å, and km s $^{-1}$ , respectively.

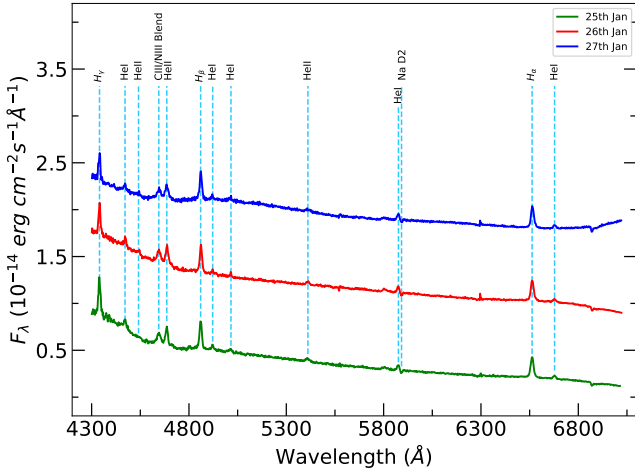


**Figure 6.** Optical spectra of V515 And obtained during three epochs. The colours represent different epochs of observations. Constants of 0.8 and 1.6 have been added to the fluxes of 26th and 27th January, respectively. Identified frequencies are marked with vertical dashed lines.

Balmer decrement (ratio of H $\beta$  to H $\alpha$  flux) values were 1.083, 1.048, and 1.002 on the three nights, respectively. The average ratio of HeII to H $\beta$  on three nights was  $\sim 0.6$ .

#### 4 DISCUSSION

A detailed timing analysis of V515 And has been performed using the high-cadence optical photometric data obtained from TESS. We have obtained the  $P_\omega$  and  $P_{\omega-\Omega}$  as  $465.4721 \pm 0.0003$  s and  $488.6067 \pm 0.0004$  s, respectively, which is in agreement with the earlier reported periods (Bikmaev et al. 2006; Butters et al. 2008). We obtained a  $P_\Omega$  of  $2.73116 \pm 0.00004$  h, hence confirming its existence in the period gap. This makes V515 And the second confirmed IP to lie in the period gap after the Paloma (Schwarz et al. 2007; Joshi et al. 2016). The spin period of Paloma (Littlefield et al. 2023) is much longer than that of V515 And, whereas their orbital periods are very close to each other.

We explain the accretion mechanism based on the strength of  $\omega$ ,  $\omega - \Omega$ , and their harmonics in the power spectra as discussed in Wynn & King (1992); Ferrario & Wickramasinghe (1999). They showed that the modulation on the  $\omega$  frequency is related to disc-fed accretion, whereas the  $\omega - \Omega$  frequency presence is suggestive of

stream-fed accretion. However, the presence of both  $\omega$  and  $\omega - \Omega$  frequencies is indicative of disc-overflow accretion (Hellier 1991, 1993b). The  $\Omega$  frequency in the power spectra can be attributed to the obscuration of the WD by the material rotating in the binary frame or the eclipse of the hotspot by the secondary (Warner 1986).

The dominance of the power of  $\omega$  and  $\omega - \Omega$  frequencies was found to switch among different sectors, indicating a change between disc-fed and stream-fed dominance in the system V515 And. In sectors 17 and 57,  $\omega$  frequency was found to be dominant, suggesting disc-fed dominance, whereas in sector 84, the  $\omega - \Omega$  frequency became dominant, resulting in stream-fed dominance. The stream-fed dominance sustained up to the middle of sector 85, after which the accretion again changed to disc-fed dominance. This type of changing accretion geometry has also been observed in other IPs like V2400 Oph (Joshi et al. 2019; Langford et al. 2022), FO Aqr (Hameury & Lasota 2017; Littlefield et al. 2020), TX Col (Rawat et al. 2021; Littlefield et al. 2021; Pandey et al. 2024), V902 Mon (Rawat et al. 2022), V709 Cas (Rao et al. 2026), etc. The most likely reason for this change could be due to the variations in the mass accretion rate (de Martino et al. 1995; Buckley 1996; de Martino et al. 1999). An enhanced mass accretion rate could cause more material to skim over the disc and directly hit the magnetosphere, resulting in stream-fed dominance, as we observe. When the mass accretion rate decreases, the amount of material accreted via stream becomes less in comparison to that accreted via disc, and we observe disc-fed dominance. Similar transitions in accretion geometry were also seen in the AAVSO-CV data by Covington et al. (2022). This changing accretion geometry trend is also reflected in the spin pulse fraction, which is higher during periods of disc-fed dominance and lower during periods of stream-fed-dominated accretion.

Upon investigating the two outbursts observed in sector 57, we determined their total durations, peak optical luminosities, and total energies. An attempt is made to classify these events into different types of outbursts. Figure 7 presents the burst duration, peak optical luminosity, and total optical energy of both outbursts, plotted on the diagnostic diagrams from Ikiewicz et al. (2024). In all three panels, the parameters of V515 And overlap with the region corresponding to recently proposed micronova candidates. Micronovae are hypothesised to be localised thermonuclear events, resulting from the unstable nuclear burning of hydrogen that has accumulated on the poles of the WD (Scaringi et al. 2022b). These bursts have also been observed in other CVs such as TV Col, EI UMa, ASASSN-19bh (Scaringi et al. 2022b), CP Pup (Veresvarska et al. 2024), PBC J0801.2-4625 (Irving et al. 2024), DW Cnc (Veresvarska et al. 2025), in which TV Col, EI UMa, and DW Cnc are IPs, and ASASSN-19bh and PBC J0801.2-4625 are also highly likely to be IPs. This supports

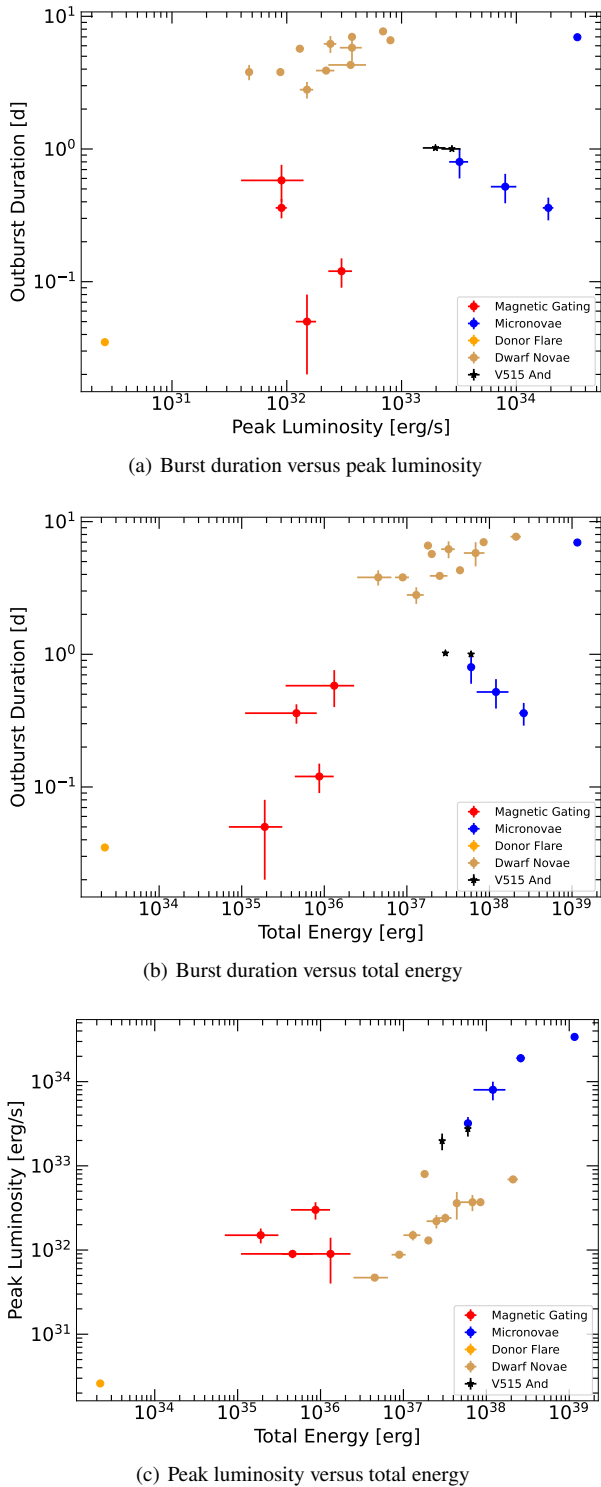


**Figure 7.** Burst properties of CVs as adapted from Figure 2 of [Iłkiewicz et al. \(2024\)](#). The outburst properties of V515 And are shown in black markers.

the necessary requirement of magnetic confinement of accreting material onto small regions ([Scaringi et al. 2022a](#)). Systems such as TV Col ( $P_{\Omega} = 5.4864$  h; [Hellier 1993a](#)), EI Uma ( $P_{\Omega} = 6.4344$  h; [Thorstensen 1986](#)), and PBC J0801.2-4625 ( $P_{\Omega} = 5.906$ ; [Irving et al. 2024](#)) lie above the period gap and while CP Pup ( $P_{\Omega} = 1.47$  h; [Orio et al. 2009](#)), and DW Cnc ( $P_{\Omega} = 1.435$  h; [Rodríguez-Gil et al. 2004](#)) lie below the period gap. For systems above the period gap, the

dominant angular momentum loss (AML) mechanism is supposed to be magnetic braking (MB), which leads to high mass transfer rates ( $\dot{M}$ ). The model by [Scaringi et al. \(2022a\)](#) suggests that high mass accretion rates ( $\dot{m}$ ) might be favourable for triggering the micronova events.

For the systems below the period gap, the primary AML mechanism is gravitational radiation (GR). GR is not as efficient a mechanism as MB. Hence, the mass accretion rates are relatively lower. The typical mass accretion rate for IPs is of the order of  $10^{-9} M_{\odot} \text{ yr}^{-1}$  ([Suleimanov et al. 2019](#)). [Veresvarska et al. \(2024, 2025\)](#) obtained the mass accretion rate of CP Pup and DW Cnc in the order of  $10^{-10}$  and  $10^{-11} M_{\odot} \text{ yr}^{-1}$ , respectively. As V515 And lies in the period gap, it is expected to have an even lesser mass accretion rate; however, [Suleimanov et al. \(2019\)](#) estimated the mass accretion rate of V515 And as  $2 \times 10^{-9} M_{\odot} \text{ yr}^{-1}$ . A high mass accretion rate is necessary to build up a critical mass of hydrogen ( $M_{crit}$ ) that can trigger the burst. It is necessary to note that the mass transfer rate and mass accretion rate may not be the same, as some amount of material may undergo lateral spreading at the base of the magnetically confined poles or be accreted outside the magnetically confined poles or both ([Scaringi et al. 2022a](#)). Based on the formulations in [Scaringi et al. \(2022a\)](#), despite having a lower mass accretion rate, an outburst may still be possible in V515 And if the magnetic confinement is confined to a very small region.

Optical spectra show hydrogen Balmer lines, along with He I and He II lines, in the emission. The He II 4686 line is typically emitted from the inner accretion disc very close to the WD, or in the vicinity of the accretion column/curtain in the case of MCVs. The varying flux and FWHM trends suggest that there could be instabilities in this region, where the emitting region is becoming less energetic or smaller, or vice versa, while the gas velocities increase as it spirals closer to the WD. During the three nights, the invert Balmer decrement is found, indicating a high density and high optical depth accretion disc. The average ratio of HeII to H $\beta$  was greater than 0.4, indicating a magnetic nature of V515 And ([Silber 1992](#)).

## 5 CONCLUSIONS

The long-term photometric TESS and ground-based optical spectroscopic observations of V515 And lead us to the following conclusions:

- Using extensive TESS observations, we derive the orbital, spin and beat period of V515 And to be  $2.73116 \pm 0.00004$  h,  $465.4721 \pm 0.0003$  s, and  $488.6067 \pm 0.0004$  s, respectively. The detection of the orbital period of V515 And confirms its location in the period gap of  $P_{\omega} - P_{\omega - \Omega}$  plane.
- The system displays a disc-overflow accretion geometry, with the relative dominance of disc-fed and stream-fed accretion varying among sectors and within individual sectors.
- Two outburst events are detected during the TESS observations with burst durations of approximately one day. Given their peak optical luminosities on the order of  $10^{33} \text{ erg s}^{-1}$ , total energies around  $10^{37}$  erg, and burst duration of  $\sim 1$  day, both events can be classified as micronova.
- Instabilities in the inner accretion disc are evident from varying flux levels of the He II 4686 line, and increasing FWHM points to a shrinking but faster-moving emitting region.

## ACKNOWLEDGEMENTS

This paper includes data collected by the TESS mission funded by NASA's Science Mission Directorate. The study utilizes data from the 3.6 m Devasthal Optical Telescope (DOT), a National Facility, operated and overseen by the Aryabhata Research Institute of Observational Sciences (ARIES), an autonomous Institute under the Department of Science and Technology, Government of India. Gratitude is extended to the scientific and technical personnel at ARIES DOT for their invaluable assistance. AJ acknowledges support from the Centro de Astrofísica y Tecnologías Afines (CATA) fellowship via grant Agencia Nacional de Investigación y Desarrollo (ANID), BASAL FB2100. We acknowledge the referee for reading our manuscript.

## DATA AVAILABILITY

The TESS data sets are publicly available in the TESS data archive at <https://archive.stsci.edu/missions-and-data/teess>. The optical spectroscopic data underlying this article will be shared on reasonable request to the corresponding author.

## REFERENCES

- Aizu K., 1973, *Progress of Theoretical Physics*, **49**, 1184
- Bikmaev I. F., Revnivtsev M. G., Burenin R. A., Sunyaev R. A., 2006, *Astronomy Letters*, **32**, 588
- Bonnet-Bidaud J. M., de Martino D., Mouchet M., 2009, *The Astronomer's Telegram*, **1895**, 1
- Bruch A., 2025, *ApJS*, **279**, 48
- Buckley D. A. H., 1996, in Evans A., Wood J. H., eds, *Astrophysics and Space Science Library* Vol. 208, IAU Colloq. 158: Cataclysmic Variables and Related Objects. p. 185, doi:10.1007/978-94-009-0325-8\_55
- Butters O. W., Norton A. J., Hakala P., Mukai K., Barlow E. J., 2008, *A&A*, **487**, 271
- Covington A. E., et al., 2022, *ApJ*, **928**, 164
- Cropper M., Wu K., Ramsay G., Kocabiyyik A., 1999, *MNRAS*, **306**, 684
- Ferrario L., Wickramasinghe D. T., 1999, *MNRAS*, **309**, 517
- Gaia Collaboration et al., 2023, *A&A*, **674**, A1
- Hameury J. M., Lasota J. P., 2017, *A&A*, **606**, A7
- Hellier C., 1991, *MNRAS*, **251**, 693
- Hellier C., 1993a, *MNRAS*, **264**, 132
- Hellier C., 1993b, *MNRAS*, **265**, L35
- Hellier C., Mason K. O., Cropper M., 1989a, *MNRAS*, **237**, 39P
- Hellier C., Mason K. O., Smale A. P., Corbet R. H. D., O'Donoghue D., Barrett P. E., Warner B., 1989b, *MNRAS*, **238**, 1107
- Ilkiewicz K., Scaringi S., Veresvarska M., De Martino D., Littlefield C., Knigge C., Paice J. A., Sahu A., 2024, *ApJ*, **962**, L34
- Irving Z. A., Altamirano D., Scaringi S., Veresvarska M., Knigge C., Castro Segura N., De Martino D., Ilkiewicz K., 2024, *MNRAS*, **530**, 3974
- Jenkins J. M., et al., 2016, in Chiozzi G., Guzman J. C., eds, *Society of Photo-Optical Instrumentation Engineers (SPIE) Conference Series* Vol. 9913, *Software and Cyberinfrastructure for Astronomy IV*. p. 99133E, doi:10.1117/12.2233418
- Joshi A., Pandey J. C., Singh K. P., Agrawal P. C., 2016, *ApJ*, **830**, 56
- Joshi A., Pandey J. C., Singh H. P., 2019, *AJ*, **158**, 11
- Kálmán S., Csizmadia S., Pál A., Szabó G. M., 2025, *Research Notes of the American Astronomical Society*, **9**, 33
- Kolb U., 1993, *A&A*, **271**, 149
- Kozhevnikov V. P., 2012, *MNRAS*, **422**, 1518
- Kumar B., et al., 2018, *Bulletin de la Societe Royale des Sciences de Liege*, **87**, 29
- Langford A., Littlefield C., Garnavich P., Kennedy M. R., Scaringi S., Szkody P., 2022, *AJ*, **163**, 4
- Littlefield C., et al., 2020, *ApJ*, **896**, 116
- Littlefield C., Scaringi S., Garnavich P., Szkody P., Kennedy M. R., Ilkiewicz K., Mason P. A., 2021, *AJ*, **162**, 49
- Littlefield C., et al., 2023, *AJ*, **165**, 43
- Lomb N. R., 1976, *Ap&SS*, **39**, 447
- Omar A., Kumar T. S., Krishna Reddy B., Pant J., Mahto M., 2019, *arXiv e-prints*, p. arXiv:1902.05857
- Orio M., Mukai K., Bianchini A., de Martino D., Howell S., 2009, *ApJ*, **690**, 1753
- Panchal D., Kumar T. S., Omar A., Misra K., 2023, *Journal of Astronomical Telescopes, Instruments, and Systems*, **9**, 018002
- Pandey J. C., Rawat N., Rao S. M., Joshi A., Singh S., 2024, *Bulletin de la Societe Royale des Sciences de Liege*, **93**, 243
- Patterson J., 1994, *PASP*, **106**, 209
- Rao S. M., Pandey J. C., Rawat N., Joshi A., Singh A. K., 2026, *New Astron.*, **122**, 102481
- Rawat N., Pandey J. C., Joshi A., 2021, *ApJ*, **912**, 78
- Rawat N., Pandey J. C., Joshi A., Yadava U., 2022, *MNRAS*, **512**, 6054
- Ricker G. R., et al., 2015, *Journal of Astronomical Telescopes, Instruments, and Systems*, **1**, 014003
- Rodríguez-Gil P., Gänsicke B. T., Araujo-Betancor S., Casares J., 2004, *MNRAS*, **349**, 367
- Rosen S. R., Mason K. O., Cordova F. A., 1988, *MNRAS*, **231**, 549
- Scargle J. D., 1982, *ApJ*, **263**, 835
- Scargle J. D., 1998, *ApJ*, **504**, 405
- Scargle J. D., Norris J. P., Jackson B., Chiang J., 2013, *arXiv e-prints*, p. arXiv:1304.2818
- Scaringi S., Groot P. J., Knigge C., Lasota J. P., de Martino D., Cavecchi Y., Buckley D. A. H., Camisassa M. E., 2022a, *MNRAS*, **514**, L11
- Scaringi S., et al., 2022b, *Nature*, **604**, 447
- Schreiber M. R., Belloni D., Schwöpe A. D., 2024, *A&A*, **682**, L7
- Schwarz R., Schwöpe A. D., Staude A., Rau A., Hasinger G., Urrutia T., Motch C., 2007, *A&A*, **473**, 511
- Silber A. D., 1992, PhD thesis, Massachusetts Institute of Technology
- Suleimanov V. F., Doroshenko V., Werner K., 2019, *MNRAS*, **482**, 3622
- Thorstensen J. R., 1986, *AJ*, **91**, 940
- Tody D., 1986, in Crawford D. L., ed., *Society of Photo-Optical Instrumentation Engineers (SPIE) Conference Series* Vol. 627, *Instrumentation in astronomy VI*. p. 733, doi:10.1117/12.968154
- Tody D., 1993, in Hanisch R. J., Brissenden R. J. V., Barnes J., eds, *Astronomical Society of the Pacific Conference Series* Vol. 52, *Astronomical Data Analysis Software and Systems II*. p. 173
- Vaughan S., 2005, *A&A*, **431**, 391
- Veresvarska M., Scaringi S., Hagen S., De Martino D., Done C., Ilkiewicz K., Knigge C., Littlefield C., 2024, *MNRAS*, **529**, 664
- Veresvarska M., et al., 2025, *MNRAS*, **539**, 2424
- Warner B., 1986, *MNRAS*, **219**, 751
- Warner B., Wickramasinghe D. T., 1991, *MNRAS*, **248**, 370
- Wu K., Chanmugam G., Shaviv G., 1994, *ApJ*, **426**, 664
- Wynn G. A., King A. R., 1992, *MNRAS*, **255**, 83
- de Martino D., Buckley D. A. H., Mouchet M., Mukai K., 1995, *A&A*, **298**, L5
- de Martino D., Silvotti R., Buckley D. A. H., Gänsicke B. T., Mouchet M., Mukai K., Rosen S. R., 1999, *A&A*, **350**, 517